

ARTICLE OPEN

Quasi-one-dimensional superconductivity in the pressurized charge-density-wave conductor HfTe₃Z. Y. Liu^{1,2,7}, J. Li^{2,3,6,7}, J. F. Zhang^{4,7}, J. Li^{2,3}, P. T. Yang², S. Zhang^{1,2,3}✉, G. F. Chen^{1,2,3}, Y. Uwatoko^{1,5}, H. X. Yang^{2,3}, Y. Sui¹✉, K. Liu⁴✉ and J.-G. Cheng^{1,2,3}✉

HfTe₃ single crystal undergoes a charge-density-wave (CDW) transition at $T_{\text{CDW}} = 93$ K without the appearance of superconductivity (SC) down to 50 mK at ambient pressure. Here, we determined its CDW vector $q = 0.91(1) a^* + 0.27(1) c^*$ via low-temperature transmission electron microscope and then performed comprehensive high-pressure transport measurements along three major crystallographic axes. Our results indicate that the superconducting pairing starts to occur within the quasi-one-dimensional (Q1D) -Te₂-Te₃- chain at 4–5 K but the phase coherence between the superconducting chains cannot be realized along either the *b*- or *c*-axis down to at least 1.4 K, giving rise to an extremely anisotropic SC rarely seen in real materials. We have discussed the prominent Q1D SC in pressurized HfTe₃ in terms of the anisotropic Fermi surfaces arising from the unidirectional Te-5p_x electronic states and the local pairs formed along the -Te₂-Te₃- chains based on the first-principles electronic structure calculations.

npj Quantum Materials (2021)6:90; <https://doi.org/10.1038/s41535-021-00393-8>

INTRODUCTION

Charge-density-wave (CDW) and conventional superconductivity (SC) are both caused by strong electron-phonon coupling and Fermi surface (FS) instabilities, and thus the interplay between these two collective electronic phenomena has been a subject of extensive investigations over the past decades¹. The former usually occurs in the low-dimensional materials and involves a periodic modulation of the conduction electron density and the underlying lattice; this will open a gap over part of the FS and thus lead to reduced conductivity. In contrast, bulk SC is a macroscopic quantum phenomenon that requires phase coherence in three dimensions and it features an FS gap that results in infinite conductivity. As such, these two electronic orders are usually competing with each other. It is frequently observed in the low-dimensional CDW conductors that suppression of CDW order leads to a bulk SC. Here, we report on a rare case that an intrinsic quasi-one-dimensional (Q1D) filamentary SC emerges and persists in a relatively wide temperature/pressure range when the CDW order of HfTe₃ along the same crystallographic direction is completely suppressed by pressure.

As shown in Fig. 1a, HfTe₃ crystallizes in the TiS₃-type structure with monoclinic space group $P2_1/m$, featured by two kinds of chain-like units, i.e., the infinite prismatic (HfTe₃)_∞ chains along the *b*-axis and the almost linear chains of -Te₂-Te₃- with alternating short (2.80 Å) and long (3.07 Å) distances along the *a*-axis². The two-dimensional (2D) prism slabs in the *ab* plane are stacked along the *c*-axis through weak van der Waals (vdW) interactions. These quasi-1D and 2D structural characters have a profound impact on the physical properties of HfTe₃ at ambient pressure. Resistivity measurements on high-quality HfTe₃ single crystals reveal pronounced anisotropic behaviors and obvious anomalies in both $\rho_a(T)$ and $\rho_c(T)$ but a very weak kink-like anomaly in $\rho_b(T)$ at around 93 K². In analog with the sister

compound ZrTe₃^{3–19}, the transport anomaly at $T_{\text{CDW}} = 93$ K has been ascribed to the formation of a CDW order within the *ac*-plane⁶. Since the ρ_c is about two orders of magnitude higher than ρ_a , the CDW should have a dominant 1D character along the -Te₂-Te₃- infinite chains. However, the wavevector of the CDW order has not been determined experimentally.

For high-quality single-crystalline HfTe₃ samples, no SC was detected down to 50 mK at ambient pressure². In contrast, the polycrystalline HfTe₃ sample shows the coexistence of the CDW order below $T_{\text{CDW}} \approx 80$ K and filamentary SC with $T_c \approx 2$ K at ambient pressure². The resistivity anomaly around T_{CDW} is much reduced in comparison with that of a single crystal, implying that the emergence of SC should be correlated with the suppression of CDW, presumably due to the presence of chemical disorders or defects in the polycrystalline samples. However, the nature of the filamentary SC without magnetic and thermodynamic signatures and its relationship with CDW remains elusive so far. For the polycrystalline sample, Denholme et al.²⁰ have performed preliminary high-pressure (HP) resistivity measurements up to ~1 GPa; they observed pressure-induced enhancement of the CDW transition, but the evolution of SC and its relationship with respect to CDW was not reported²⁰. Considering the strong anisotropy of the physical properties associated with the Q1D nature of the crystal structure, it is imperative to carry out a comprehensive HP study on single-crystalline samples in order to unveil the nature of the filamentary SC and its interplay with CDW.

In this work, we first determined experimentally the CDW vector $q = 0.91(1) a^* + 0.27(1) c^*$ of HfTe₃ by low-temperature transmission electron microscope (TEM) at ambient pressure, and then performed a comprehensive HP transport study on the HfTe₃ single crystals along three major crystallographic axes. Intriguingly, we observed the emergence of an intrinsic filamentary SC in $R_a(T)$ at $T \leq 4$ –5 K when the CDW of HfTe₃ is suppressed completely by $P \geq 5$ GPa, whereas no clear sign of SC is observed

¹School of Physics, Harbin Institute of Technology, Harbin 150001, China. ²Beijing National Laboratory for Condensed Matter Physics and Institute of Physics, Chinese Academy of Sciences, Beijing 100190, China. ³School of Physical Sciences, University of Chinese Academy of Sciences, Beijing 100190, China. ⁴Department of Physics, Beijing Key Laboratory of Opto-electronic Functional Materials & Micro-nano Devices, Renmin University of China, Beijing 100872, China. ⁵Institute for Solid State Physics, University of Tokyo, Kashiwa, Chiba 277-8581, Japan. ⁶Present address: Department of Mathematics and Physics, Shijiazhuang TieDao University, Shijiazhuang 050043, China. ⁷These authors contributed equally: Z. Y. Liu, J. Li, J. F. Zhang. ✉email: szhang@iphy.ac.cn; suiyou@hit.edu.cn; kliu@ruc.edu.cn; jgcheng@iphy.ac.cn

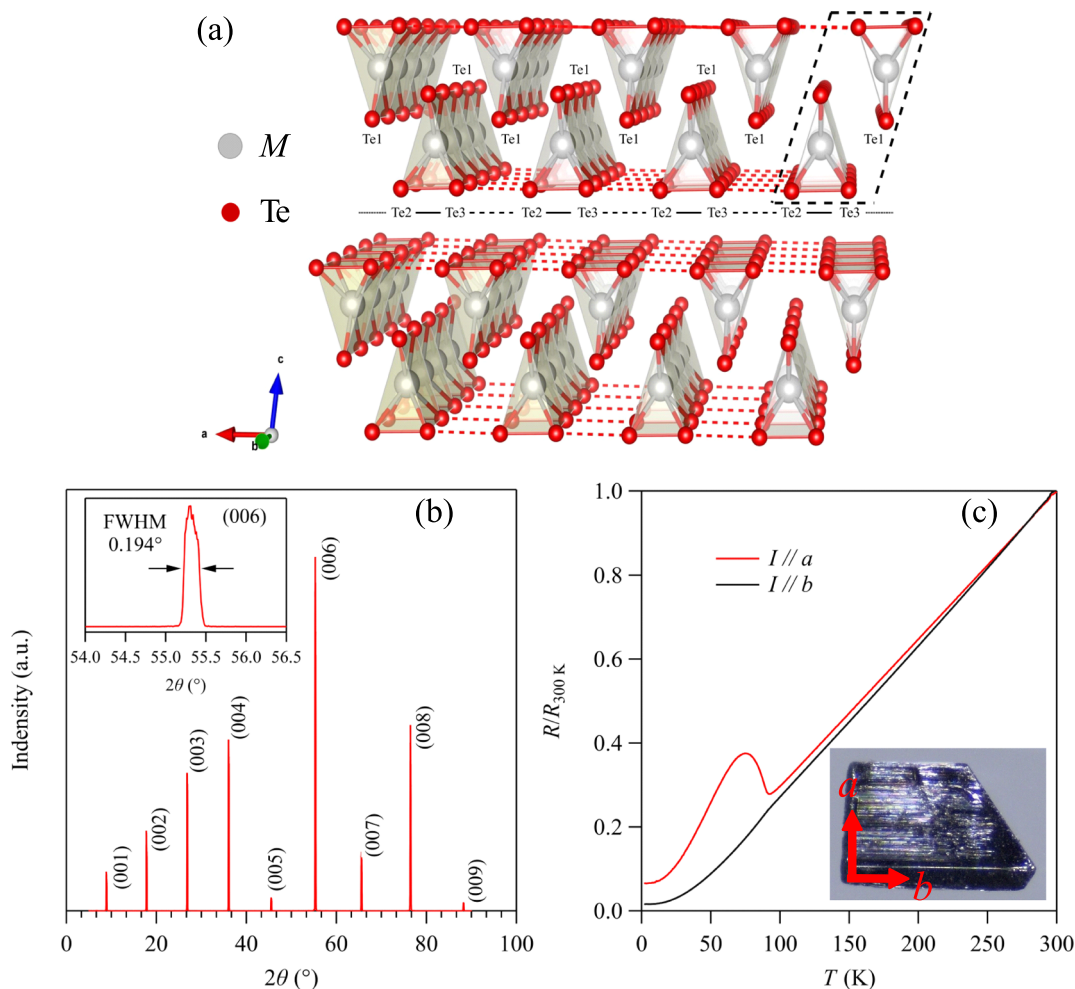


Fig. 1 Crystal structure and transport property at ambient pressure. **a** Crystal structure of $M\text{Te}_3$ ($M = \text{Zr}, \text{Hf}$). **b** X-ray diffraction pattern of the single-crystal HfTe_3 showing only the $(00l)$ diffraction peaks. The inset shows the FWHM of the (006) Bragg peak. **c** Temperature dependence of the a - and b -axis normalized resistance $R(T)/R_{300\text{K}}$ measured on the same piece of a sample at ambient pressure. Displayed in the inset of **(c)** is the photo of the crystal, which shows fringes extending along the b -axis.

down to 1.4 K in $R_b(T)$ and $R_c(T)$, demonstrating an extraordinary case of Q1D SC rarely seen in real materials. We have analyzed the excess conductivity according to the theory of Aslamazov and Larkin (A-L)²¹ and compared our results with those of ZrTe_3 ^{3–19,22}. Finally, we discussed the observed Q1D SC in terms of the anisotropic FSs and the local pairs formed along the $-\text{Te}_2\text{-Te}_3$ -chains parallel to the a -axis based on the first-principles electronic structure calculations.

RESULTS

Characterizations at ambient pressure

The single-crystal XRD pattern of HfTe_3 shown in Fig. 1b displays only the sharp $(00l)$ diffraction peaks, which confirm that the single crystals are grown along the ab plane and stacked along the c -axis. The c -axis lattice constant is determined to be $c = 10.0519 \text{ \AA}$, in consistent with the previous report². As shown in the inset of Fig. 1b, the full width at half maximum (FWHM) of the (006) Bragg peak is about 0.2° , implying a high quality of the crystals. Within the plate-like crystal surface, the a and b axes are determined to be perpendicular and parallel to the crystal edges, respectively, by the Laue back diffraction. As shown in the inset of Fig. 1c, the HfTe_3 single crystal shows fringes extending along the b -axis, which is parallel to the crystal edge. Thus, the a - and b -axis that are orthogonal with each other

within the ab plane can be distinguished visually for the as-grown crystals. For this sample, we measured the temperature dependence of anisotropic resistance $R(T)$ along the a - and b -axis, respectively. As seen in Fig. 1c, the a -axis resistance exhibits a pronounced hump anomaly at $T_{\text{CDW}} = 93 \text{ K}$ associated with the CDW transition, while the b -axis resistance shows a very weak kink-like anomaly at T_{CDW} without any trace of superconducting transition down to 1.8 K. These results agree well with the previous report². The residual resistivity ratio, $\text{RRR} \equiv R(300 \text{ K})/R(2 \text{ K})$ along the b -axis is calculated to be 62, which also highlights the high quality of the studied single-crystal sample. We have thus selected samples with similar RRR values for the HP measurements as shown in Supplementary Fig. 1.

Although it is expected that HfTe_3 should form a similar CDW as that of ZrTe_3 with $\mathbf{q} = 0.93 a^* + 0.33 c^*$, the q -vector of HfTe_3 has not been determined experimentally so far. Here we employed a low-temperature TEM to directly determine the CDW vector of the HfTe_3 single crystal. Figure 2a, b show the selected area electron diffraction (SAED) patterns of HfTe_3 taken along the $[001]$ zone axis at room temperature and 26 K, respectively. The pristine lattice at room temperature has a monoclinic structure with space group $P2_1/m$, and the satellite spots can only be identified below the CDW phase transition temperature. As shown in the inset of Fig. 2b, the intensity of the satellite spot goes up as the scattering angle increases and reaches a maximum at 17.5 mrad,

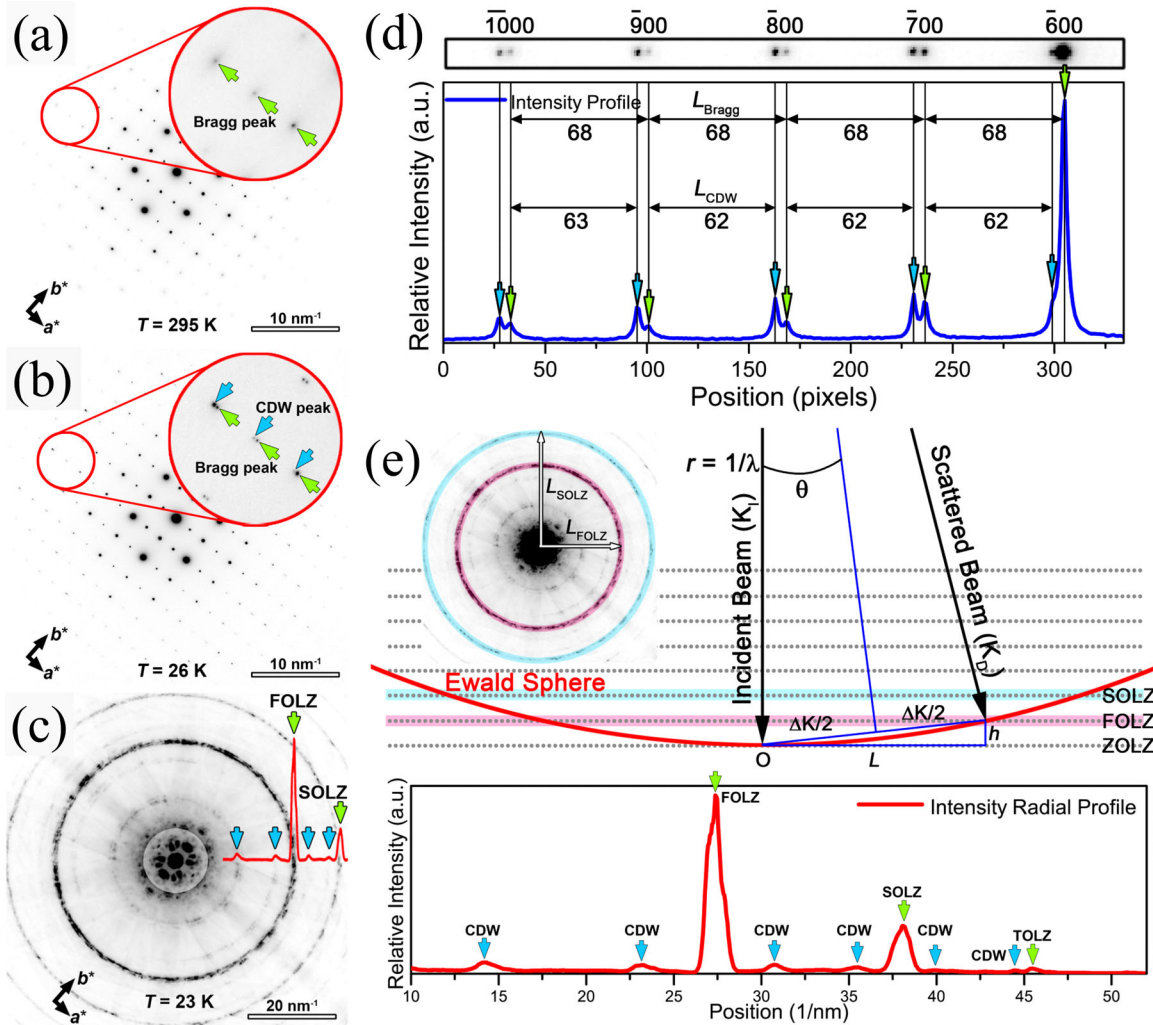


Fig. 2 Electron diffraction patterns of HfTe_3 . Typically selected area electron diffraction (SAED) patterns taken along the [001] zone axis at **a** 295 K and **b** 26 K, respectively. The satellite spots (indicated by blue arrows) appear at low temperatures around the Bragg spots (green arrows), indicating the formation of structural modulation. **c** A convergent beam electron diffraction (CBED) pattern taken along the [001] zone axis, showing extra Laue zones (blue arrows) due to the structural modulation. The radial intensity distribution is plotted as an inset, with the positions of the first/second-order Laue zone (FOLZ/SOLZ) indicated by green arrows. Based on **(b)** and **(c)**, the modulation vector can be determined to be $\mathbf{q} = 0.91(1)\mathbf{a}^* + 0.27(1)\mathbf{c}^*$. **d** Intensity line profile from spot $(\bar{6}00)$ to $(\bar{1}000)$ extracted from the SAED pattern **(b)**. The intervals between different spots are labeled. **e** Upper panel: the geometric configuration showing the Ewald sphere intercepts points in the Laue zones. Lower panel: the intensity radial profile extracted from CBED pattern **(c)**, from which the L values can be obtained.

indicating that the structural modulation vector \mathbf{q} has both \mathbf{a}^* and \mathbf{c}^* components, i.e., $\mathbf{q} = q_a \mathbf{a}^* + q_c \mathbf{c}^*$. The extra Laue zones (indicated by blue arrows) presented in the [001] CBED pattern, Fig. 2c, further confirm that the modulation vector does not lie in the ab plane.

In order to determine the value of q_a and q_c , the intensity distributions of CDW spots/rings in Fig. 2b, c are summarized in Fig. 2d, e, respectively. Figure 2d shows the line intensity profile from spot $(\bar{6}00)$ to $(\bar{1}000)$, in which the intervals between adjacent Bragg spots (L_{Bragg}) and the distance from one Bragg spot to the next-nearest CDW neighbor (L_{CDW}) are labeled. Using $q_a = L_{\text{CDW}}/L_{\text{Bragg}}$, q_a is calculated to be 0.91(1). On the other hand, the value of q_c can be estimated with the aid of the geometric configuration presented in Fig. 2e. The positions of the rings in Fig. 2c are directly related to the interception of the Ewald sphere with the Laue zone layers. For high-energy electrons, we can write an expression for the angle θ in Fig. 2e: $\sin\theta = \frac{\Delta K/2}{r} = \frac{h}{\Delta K}$. Using the equation $(\Delta K)^2 = h^2 + L^2$, we have $h = r - \sqrt{r^2 - L^2}$, where r is the radius of the Ewald sphere ($r = 398.74 \text{ nm}^{-1}$ when the

electron energy is 200 keV). The L values for different rings can be obtained from the radial profile plotted in the low panel of Fig. 2e. Then, by calculating h for different Laue zones and the ratios (for example $q_c = h_{\text{CDW}}/h_{\text{FOLZ}}$, where h_{CDW} and h_{FOLZ} are the h values for the innermost ring and the FOLZ ring, respectively), q_c is estimated to be 0.27(1). Thus, we can write $\mathbf{q} = 0.91(1)\mathbf{a}^* + 0.27(1)\mathbf{c}^*$.

To further understand the temperature-dependent behavior of the structural modulation, we acquired SAED patterns at several different temperatures, as shown in Supplementary Fig. 2. It is evident that the superlattice spots (indicated by blue arrows) become dim at 81 K and totally disappear at 88 K, showing good agreement with the CDW phase transition temperature determined from the resistivity measurements. The result suggests that the superlattice spots observed in diffraction patterns are directly related to the formation of the CDW phase.

It is worth noting that the satellite spots appeared in the electron diffraction patterns of ZrTe_3 at room temperature. Eaglesham et al.⁶ believed that the satellite spots at room temperature indicated the composition modulation of ZrTe_3

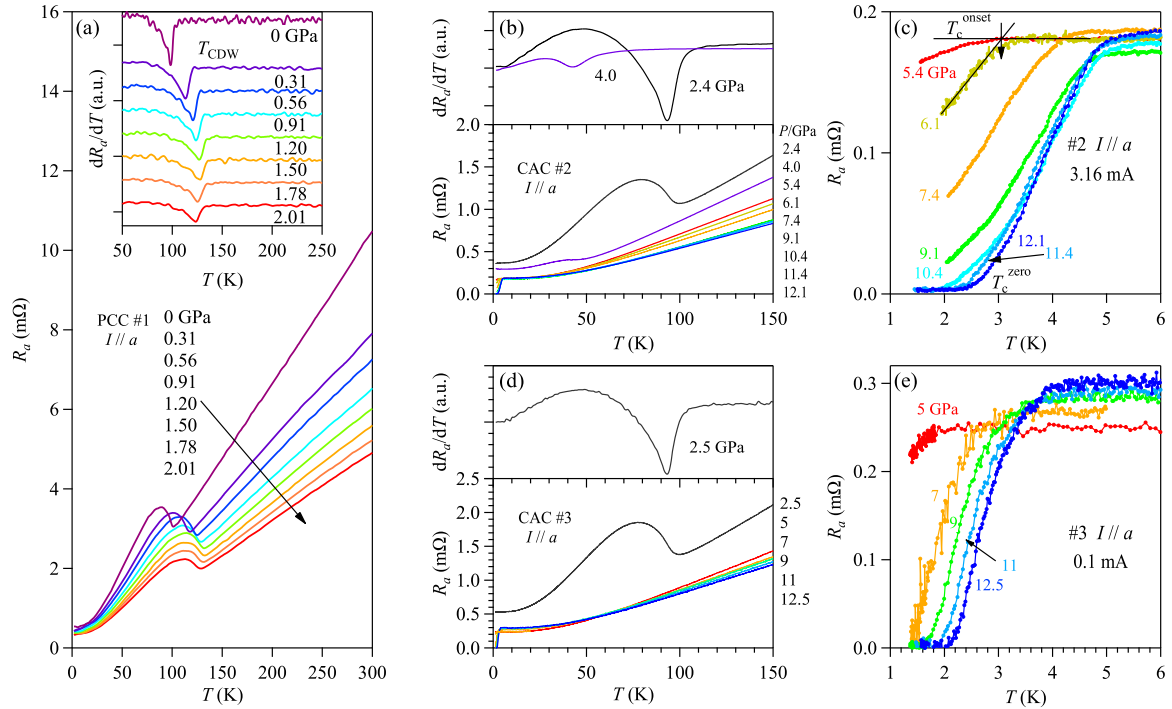


Fig. 3 The a -axis resistance under high pressure. **a** Temperature dependence of the a -axis resistance $R_a(T)$ for sample #1 under various pressures up to 2.01 GPa measured with a piston-cylinder cell (PCC); the inset shows the dR_a/dT of the data in **(a)** to determine the charge-density-wave transition temperature T_{CDW} . **b** $R_a(T)$ for sample #2 under various pressures from 2.4 to 12.1 GPa measured with a palm cubic anvil cell (CAC); the upper panel shows the dR_a/dT curves at 2.4 and 4.0 GPa to determine the values of T_{CDW} . **c** The low-temperature $R_a(T)$ for sample #2 under various pressure from 5.4 to 12.1 GPa. **d** $R_a(T)$ for sample #3 under various pressures from 2.5 to 12.5 GPa; the upper panel shows the dR_a/dT curve at 2.5 GPa to determine the values of T_{CDW} . **e** The low-temperature $R_a(T)$ for sample #3 under various pressure from 5 to 12.5 GPa highlighting the evolution of the possible superconducting transition.

caused by off-stoichiometry. This is also considered to be a strong evidence that the quality of $ZrTe_3$ crystals is difficult to control. For the $HfTe_3$ single crystal, we can see that the SAED patterns do not show any satellite spots at room temperature, which indicates that the crystal structure of the $HfTe_3$ single crystal is perfect and closer to the stoichiometry.

Effect of pressure on the a -axis resistance

Figure 3a shows the temperature dependence of the a -axis resistance $R_a(T)$ of the $HfTe_3$ single crystal (#1) under various pressures up to 2.0 GPa measured with a PCC. Details about the experimental setup for anisotropic resistance measurements can be found in Supplementary Fig. 4. At ambient pressure, $R_a(T)$ displays a hump anomaly due to the CDW formation at $T_{CDW} = 93$ K, which can be determined from the minimum of dR_a/dT as shown in the inset of Fig. 3a. With increasing pressure, T_{CDW} first moves to higher temperatures, reaching the maximum of ~ 128 K at 1.5 GPa, and then decreases gradually to 122.4 K at 2.01 GPa. The jump of $R_a(T)$ around T_{CDW} is reduced gradually accompanying the suppression of CDW transition. Such a non-monotonic variation of $T_{CDW}(P)$ has also been observed in $ZrTe_3$ ¹², and thus should have an origin in common. The initial enhancement of T_{CDW} at low pressures indicates that the lattice compression first prompts the CDW formation, presumably due to the enhancement of electron-lattice coupling or the optimization of the nesting condition for the parallel FSs along the a^* -axis. Nonetheless, the CDW should be eventually suppressed by pressure as observed in $ZrTe_3$ ¹².

The evolution of the CDW transition at $P > 2$ GPa is further investigated by measuring $R_a(T)$ of a second $HfTe_3$ crystal (#2) with a CAC. The obtained $R_a(T)$ and the selected dR_a/dT curves are displayed in Fig. 3(b). The $R_a(T)$ at 2.4 GPa is similar to that

measured in PCC, and the T_{CDW} has been further reduced to 93.8 K. When the pressure is increased to 4 GPa, the T_{CDW} is quickly lowered to 43.3 K and the resistance anomaly at T_{CDW} is significantly suppressed, as shown in Fig. 3b. At 5.4 GPa and above, no resistance anomaly can be discerned anymore at $T > 5$ K, implying the complete suppression of the CDW transition in $HfTe_3$. In this pressure range, the magnitude of $R_a(T)$ at high temperatures decreases gradually with increasing pressure while that at low temperatures keeps almost constant.

Interestingly, we observed a gradual resistance drop at low temperatures for $P > 5.4$ GPa, signaling the possible emergence of SC accompanying the elimination of CDW in $HfTe_3$. As shown in Fig. 3c, the enlarged view of $R_a(T)$ at $T \leq 6$ K evidences a slight downturn feature below $T_c^{\text{onset}} \approx 3$ K at 5.4 GPa. Upon further increasing pressure, the drop of resistance becomes stronger and the T_c^{onset} moves gradually to higher temperatures, reaching a nearly constant value of ~ 5 K at $P \geq 9.1$ GPa. The zero resistance is finally achieved at $T_c^{\text{zero}} \approx 2$ –2.5 K at $P \geq 11.4$ GPa. We found that the resistance drop in $R_a(T)$ can be suppressed by applying either high electric currents and/or external magnetic fields, as seen in Fig. 4a, b). These observations are consistent with the occurrence of SC in $HfTe_3$ at $P \geq 5.4$ GPa when the CDW transition along the a -axis is suppressed completely. It should be noted that the resistance data became too noisy under magnetic fields higher than 0.3 T, which prevented us from determining precisely the upper critical field.

In order to ensure the reproducibility of the experimental results, we performed HP resistance measurements on a third $HfTe_3$ (#3) single crystal along the a -axis. As shown in Fig. 3d, e, the CDW transition at 93 K is clearly observed for $R_a(T)$ at 2.5 GPa and is completely suppressed at 5 GPa; the SC transition is also confirmed at low temperature for $P \geq 5$ GPa. It is noted that the observed T_c for this sample is slightly lower than that of sample #2,

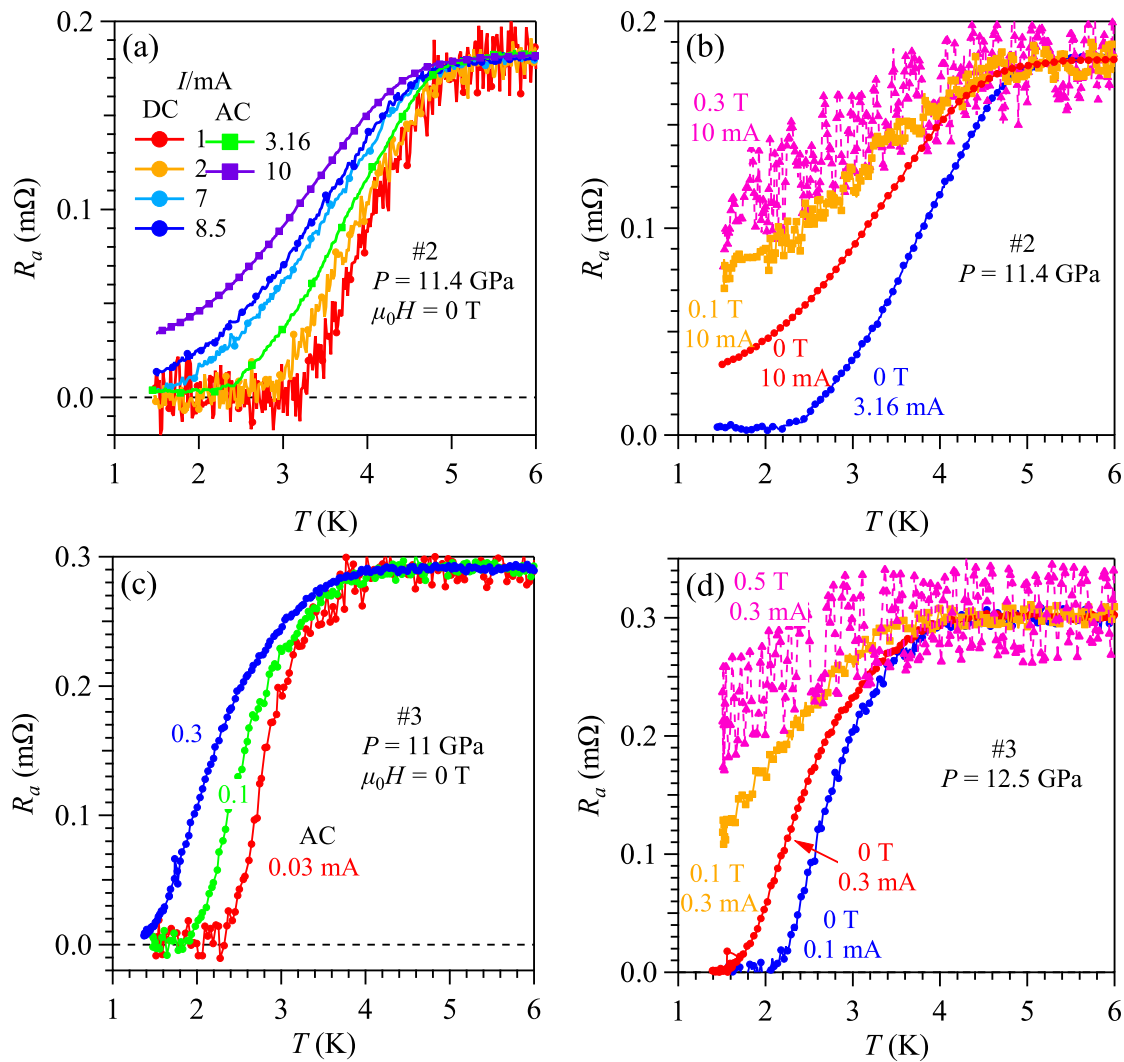


Fig. 4 The low-temperature a -axis resistance under high pressure. The low-temperature $R_a(T)$ for sample #2 at 11.4 GPa was measured with **a** different currents and **b** magnetic fields. **c** The low-temperature $R_a(T)$ for #3 at 11 GPa was measured with different currents. **d** The low-temperature $R_a(T)$ for #3 at 12.5 GPa measured with different currents and/or magnetic fields.

implying that the pressure-induced SC in HfTe_3 is sensitive to the sample quality. As shown in Supplementary Fig. 5, the RRR values of sample #2 are indeed larger than those of sample #3 in the pressure range when CDW is suppressed completely. Accordingly, the T_c^{onset} of sample #2 is also higher than that of sample #3. Nevertheless, the results of sample #3 are in general agreement with those of the #2 sample. Furthermore, we also measured the low-temperature resistance at 11 and 12.5 GPa under different electric currents and external magnetic fields. As shown in Fig. 4c, d, the gradual suppression of the $R_a(T)$ drop upon applying high electric currents and/or external magnetic fields further substantiates the emergence of pressure-induced SC in HfTe_3 along the a -axis.

To verify if the observed SC is bulk or not, we have attempted to measure the ac magnetic susceptibility $\chi'(T)$ of HfTe_3 together with a piece of Pb as a superconducting reference in the CAC up to 12 GPa. As shown in Supplementary Fig. 6, no obvious diamagnetic signal was observed for HfTe_3 down to 1.4 K, except for the superconducting transition of Pb, which shifts to lower temperatures progressively with increasing pressure. The observed sharp transitions of Pb in Supplementary Fig. 6 elaborate an excellent hydrostatic pressure condition in the CAC at least up to 12 GPa. The absence of obvious diamagnetic response thus indicates a

non-bulk or filamentary nature for the observed SC in HfTe_3 at least down to 1.4 K. This observation motivated us to further investigate the effect of pressure on the b - and c -axis resistances, which lead to very surprising results as shown below.

Effect of pressure on the b -axis resistance

Because the samples #2 and #3 measured above are always disassembled into many filaments after decompression from high pressures, presumably due to the special sample microstructure and the presence of residual stress upon compression. This issue prevents the subsequent measurements along the b -axis direction on the identical samples. Under such a circumstance, we selected another two HfTe_3 samples #4 and #5 for measurements of the b -axis resistance $R_b(T)$ in two separated runs in the pressure range 7–12.5 GPa, where zero resistance can be achieved in $R_a(T)$. The results of $R_b(T)$ for these two samples are shown in Fig. 5a. As seen clearly, the $R_b(T)$ curves of both samples do not exhibit any anomaly at the temperatures of ~ 4 –5 K where $R_a(T)$ starts to show the superconducting transition. For sample #5, we observed a slight downturn of $R_b(T)$ starting at $T < 2$ K under $P \geq 10$ GPa, Fig. 5b, which is likely caused by some misalignment of the electrical contact so that some a -axis component was picked up.

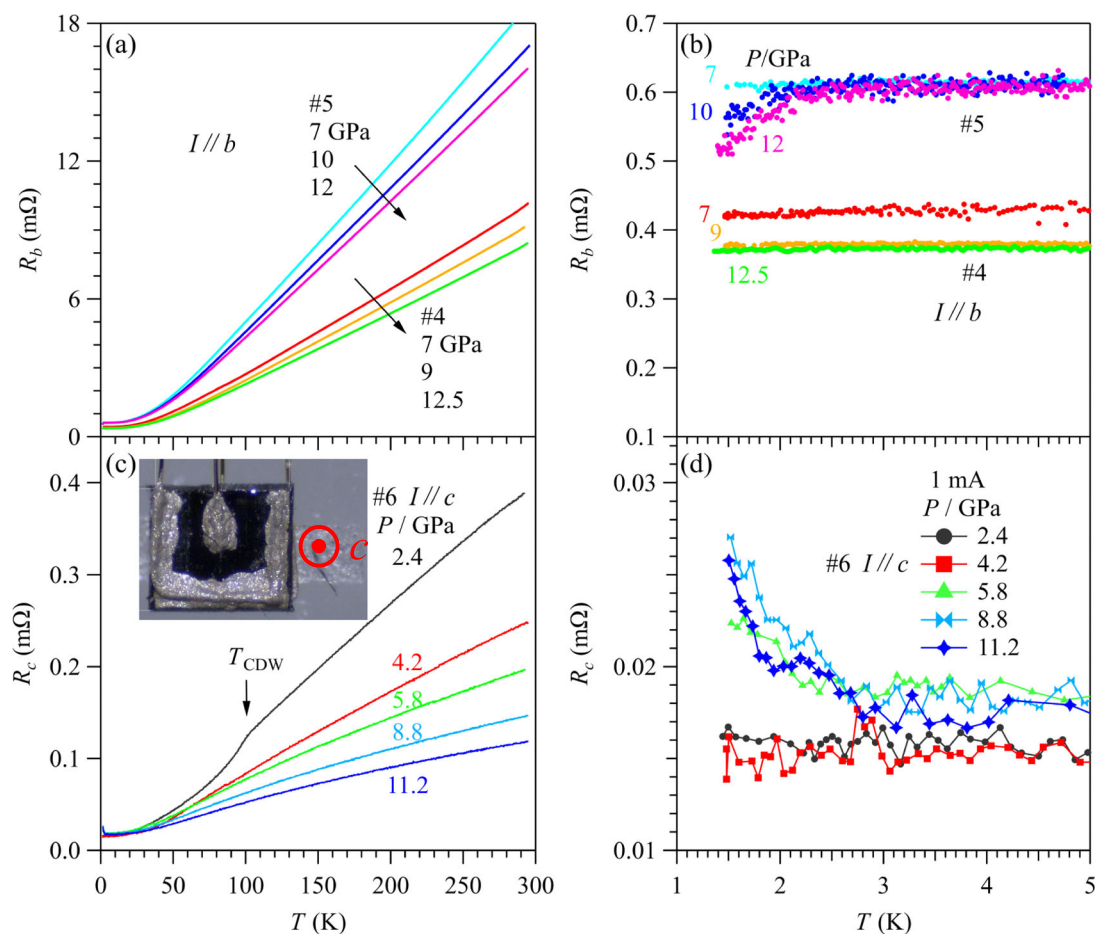


Fig. 5 The *b*- and *c*-axis resistance under high pressure. **a** The temperature dependence of *b*-axis resistance $R_b(T)$ under different pressures from 7 to 12.5 GPa for two samples (#4 and #5) and **b** their low-temperature data. **c** The temperature dependence of *c*-axis resistance $R_c(T)$ under different pressures from 2.5 to 11 GPa for sample #6 and **d** their low-temperature parts below 5 K. The inset of **(c)** shows the photo of the sample for the resistance measurement along *c*-axis.

These results are striking. First of all, they immediately exclude the possibility that the pressure-induced resistivity drop in $R_a(T)$ arises from a secondary phase. Secondly, the observed SC in $R_a(T)$ is very likely a Q1D phenomenon. As shown below, our simulations with a 2D resistor matrix can well reproduce the above $R_b(T)$ results. To substantiate this conclusion, we further measured the *c*-axis resistance $R_c(T)$ under various pressures.

Here, we want to point out that it is quite challenging experimentally to collect merely the *b*-axis resistance without any *a*-axis contribution for the resistance measurements on a bulk sample. This is particularly difficult given the fact that the *a*-axis resistance exhibits a pronounced drop around 4–5 K whereas the *b*-axis resistance almost levels off. Therefore, a slight misalignment of the voltage leads $V+/V-$ with respect to the *a*-axis, i.e., they should be perfectly parallel with the *a*-axis, will inevitably introduce the *a*-axis feature, overshadowing the intrinsic response of *b*-axis resistance. Under such a circumstance, the chance to observe a resistivity drop along the *b*-axis is high, but it should be convincing if we can observe no obvious resistivity drop by chance. To overcome this problem, we tried to first pattern the electrical contacts by evaporating the gold pads on the sample surface so as to make them as parallel to the *a*-axis as possible, see Supplementary Fig. 4b, then we attached the electrical leads with silver paste. In this way, we are able to observe no any resistance drop for sample #4 and a tiny drop for sample #5 as shown in Fig. 5b.

Effect of pressure on the *c*-axis resistance

We employed the configuration shown in the inset of Fig. 5c to measure precisely the $R_c(T)$ of the plate-like HfTe_3 crystal (#6). The electric current flows through the sample via the U-shaped $I+/I-$ pads on the opposite sides of the crystal, while the voltage leads $V+/V-$ are attached to the center pads on both sides. At ambient pressure, $R_c(T)$ exhibits an upturn upon cooling through T_{CDW} ². As seen in Fig. 5c, the resistance upturn below T_{CDW} is quickly suppressed by pressure, and the $R_c(T)$ at 2.4 GPa displays a metallic behavior in the whole temperature range with a clear kink-like anomaly at $T_{\text{CDW}} \approx 96.5$ K, which is consistent with that determined from $R_a(T)$ in Fig. 3b. The CDW transition cannot be discerned anymore at $P \geq 4.2$ GPa, implying the complete suppression of CDW by pressure. In the investigated pressure range, we observed no emergence of possible SC down to 1.4 K. Interestingly, the $R_c(T)$ curves at $P \geq 5.8$ GPa even exhibit an unusual upturn below around 2.5 K, as shown in Fig. 5d. The upward trend of $R_c(T)$ below 2.5 K is more obvious when the pressure increases to 11.2 GPa. As shown below, these results can be well accounted for by turning on a Q1D SC in the resistor-matrix model. The above results thus unambiguously demonstrate the emergence of an extremely anisotropic SC in HfTe_3 under pressures.

T-P phase diagram of HfTe_3

The pressure dependencies of T_{CDW} and T_c determined from $R_a(T)$ are shown in Fig. 6, which depicts clearly the competition

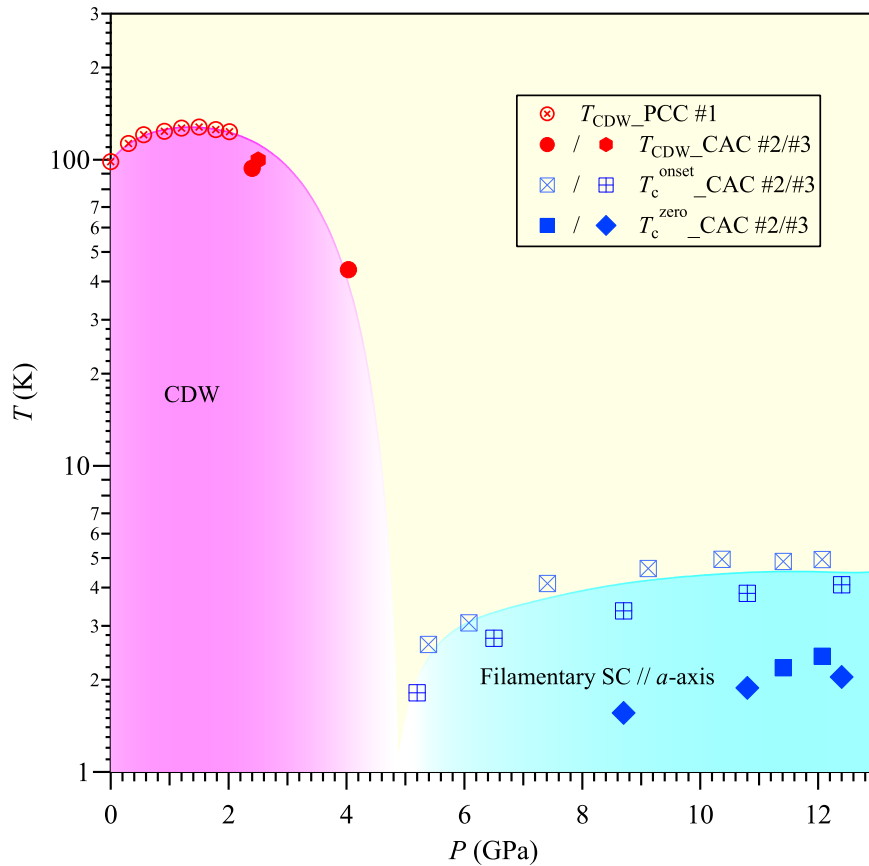


Fig. 6 Temperature-pressure phase diagram of HfTe₃ single crystal. Pressure dependences of the charge-density-wave transition temperature T_{CDW} and the superconducting transition temperatures $T_{\text{c}}^{\text{onset}}$ and $T_{\text{c}}^{\text{zero}}$ determined from the resistance measurements along the a -axis.

between CDW and the possible Q1D SC along the a -axis. With increasing pressure, T_{CDW} initially increases, reaching a broad maximum at 1.5 GPa, then decreases quickly and vanishes completely at about 5 GPa, above which the Q1D SC emerges abruptly. The $T_{\text{c}}^{\text{onset}}$ increases gradually and reaches a nearly constant value of ~ 5 K at least up to 12 GPa. The zero resistance is eventually realized at $T_{\text{c}}^{\text{zero}} \approx 2$ K under $P > 11$ GPa, however, the diamagnetic response cannot be obtained due to the lack of phase coherence along the b - and c -axis.

Therefore, our present work not only demonstrates unambiguously a competitive nature between CDW and SC but also reveals an intriguing anisotropic SC in the pressurized HfTe₃, i.e., the Q1D SC emerges along the a -axis in a relatively broad temperature/pressure range after the CDW is completely suppressed, whereas the phase coherence between the superconducting chains cannot be realized down to 1.4 K along the other directions.

One noteworthy feature of the phase diagram shown in Fig. 6 is that SC emerges along the a -axis only after the CDW is suppressed completely by pressure without showing any coexistence region. In contrast, the polycrystalline HfTe₃ sample with a lower $T_{\text{CDW}} \approx 80$ K shows the coexistence of CDW and filamentary SC at ambient pressure². Although both the chemical disorders/defects and the physical pressure can suppress CDW and then induce SC, the above comparison actually highlights their distinct roles in tuning the CDW and SC states. In comparison with the “clean” tuning of physical pressure, the chemical disorders/defects may introduce extra charge carriers. According to the theoretical study by Imada et al.²³, the relationship between CDW and SC in a Q1D system depends sensitively on the band filling, i.e., they are separated for a half-filled band but can coexist for quarter filling. They also pointed out that the coexistence of SC and CDW in a

non-half-filled system is a general feature of anisotropic systems. It is plausible that the Q1D bands of HfTe₃ along the a -axis is close to half-filling, leading to a complete competitive relationship between SC and CDW, while the deviation from the half-filling in the polycrystalline samples gives rise to the coexistence of CDW and SC. Our simple calculations on the density of states (DOS) distribution of the $p_x/p_y/p_z$ type Wannier orbits on the -Te2-Te3-atoms seem to support such a scenario, i.e., the filling numbers of the p_x -type Wannier orbits along the 1D atom chain direction are about 0.55, Supplementary Fig. 14. It should be noted that the valence state of Te ions in HfTe₃ is complex, and more experimental and theoretical investigations are needed to understand the interplay between CDW and SC.

Crystal structure under high pressure

To study the structural stability of HfTe₃ under compression, we also measured the high-pressure XRD on the pulverized HfTe₃ crystals at room temperature and found no structure transition up to at least 14 GPa. As shown in Fig. 7, the lattice parameters a , b , c , and volume V contract smoothly with increasing pressure, implying that the crystal structure is stable in the studied pressure range. The pressure dependence of volume $V(P)$ can be well fitted with the Birch–Murnaghan (B–M) equation of state as shown by the solid line in Fig. 7b. By fixing $B_1 = 4$, we obtained a bulk modulus $B_0 = 45.3(7)$ GPa and $V_0 = 228.7(4)$ Å³. In addition, there is no obvious anomaly for the lattice parameter a at $P_c \approx 5$ GPa, where the CDW disappears and the Q1D SC emerges at low temperatures. The axial ratios c/a and b/a decrease monotonically with increasing pressure, Supplementary Fig. 7, indicating that the b and c axes are more compressible than a -axis. The smooth

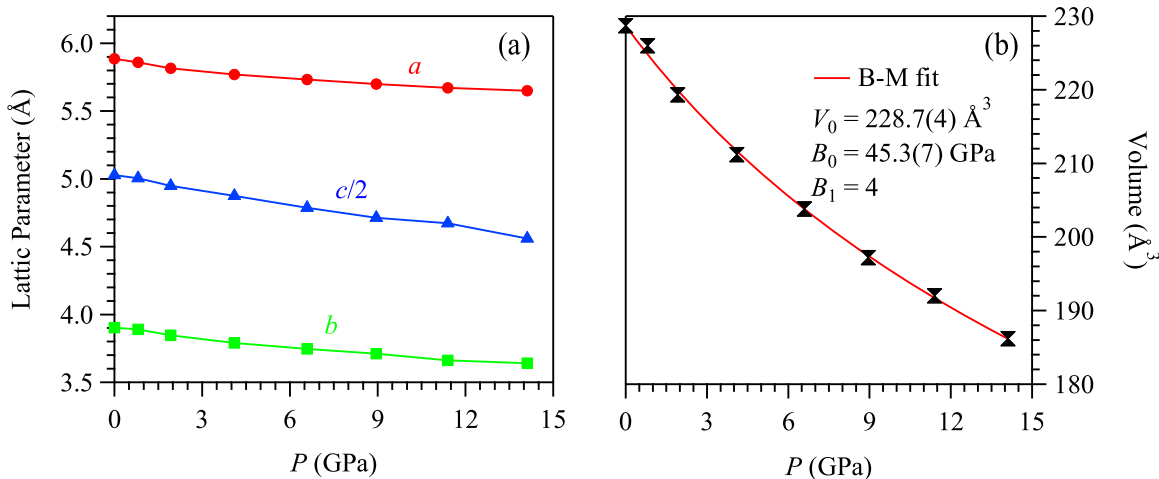


Fig. 7 Crystal-structural under high pressure. Pressure dependences of **a** the lattice parameters and **b** volume of HfTe₃ at room temperature. The solid line in **(b)** represents the fit with the Birch–Murnaghan (B–M) equation of state to extract the bulk modulus B_0 as given in the figure.

evolutions of the axial ratios c/a and b/a up to ~ 10 GPa also indicate that the crystal structure is stable within the studied pressure range. Therefore, we can safely conclude that pressure-induced SC around 5 GPa should be correlated with an electronic transition rather than a structural transition, i.e., it is linked directly with the elimination of the CDW order. In this sense, the pressure-induced SC along the a -axis can be regarded as a new electronic phase, which shares a similar crystal structure as the ambient phase but has no CDW instability.

DISCUSSIONS

In order to simulate the above anisotropic transport behaviors at low temperatures under HP, we designed a simplified 2D resistor matrix consisting of 45 resistors as shown in Supplementary Figs. 8–11. We first simulate the change of b -axis resistance R_b with a perfect alignment upon entering the superconducting state along the a -axis, manifested by a reduction of the resistors' resistance from 5 to 0.1 Ω along this direction. As shown in Supplementary Fig. 8, the voltage drop across $V+/V-$ along the b -axis (or equivalently R_b) remains unchanged when the resistance of resistors along the a -axis are reduced from 5 to 0.1 Ω , consistent with the experimental results for sample #4 in Fig. 5b. However, when the alignment of voltage leads is not perfect, some a -axis component will be picked up as simulated in Supplementary Fig. 9. In this case, the voltage drop across $V+/V-$ is found to decrease slightly when the resistors along the a -axis are reduced from 5 to 0.1 Ω . This reproduces well the observed resistance drop of sample #5 shown in Fig. 5b, confirming that the change of R_a will affect the R_b sensitively if the alignment of voltage leads is imperfect.

We further simulated the influence of resistance drop of R_a and the misalignment of $V+/V-$ on the c -axis resistance R_c . As illustrated in Supplementary Figs. 10 and 11, interestingly, the voltage drop across $V+/V-$ along the c -axis (or equivalently R_c), no matter aligned perfectly or not, was both found to rise progressively when the resistance of the resistors along the a -axis is reduced gradually, in excellent agreement with the experimental results shown in Fig. 5d. In contrast, the voltage drop will decrease if the superconducting transition takes place in the c -axis direction. The above simulations not only reproduce the experimental observations but also support strongly the occurrence of a Q1D SC in the pressurized HfTe₃ single crystal.

To further substantiate the occurrence of Q1D SC along the a -axis, we then analyzed the excess conductivity ($\Delta\sigma = \sigma - \sigma_0$)

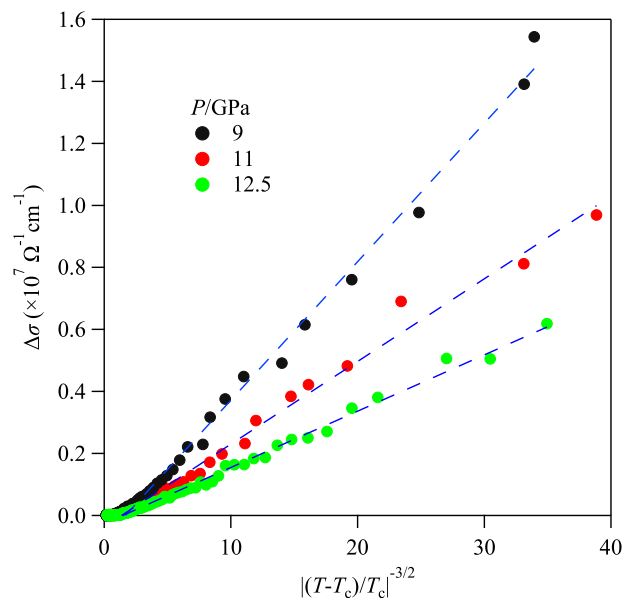


Fig. 8 Analysis with the Aslamazov and Larkin (A-L) model. The reduced temperature dependence of excess conductivity $\Delta\sigma$ along the a -axis.

around T_c according to A-L model²¹, viz.

$$\Delta\sigma \propto [(T - T_c)/T_c]^{-(4-D)/2} \quad (1)$$

where D is the dimensionality and T_c is the mean-field transition temperature, which equals to T_c^{zero} . For $D=1$, the excess conductivity due to 1D superconducting fluctuations is given by:

$$\Delta\sigma = (\pi e^2/16hd^2)\xi(0)[(T - T_c)/T_c]^{-3/2} \quad (2)$$

Here, e is the electron charge, d is the diameter of a superconducting filament, and $\xi(0)$ is the coherence length at $T=0$ K. As illustrated in Fig. 8, the excess conductivity $\Delta\sigma$ from 9 to 12.5 GPa for sample #3 measured at a smaller current 0.1 mA indeed follows a nice linear relationship as a function of $[(T - T_c)/T_c]^{-3/2}$; here the $\Delta\sigma$ is calculated from data shown in Fig. 3e and σ_0 is the conductivity at 6 K for $l//a$ with 0.1 mA current. These observations indicate that strong 1D superconducting fluctuations persist even up to 12.5 GPa. It is also noteworthy that the slope of the fitting curve decreases gradually with increasing

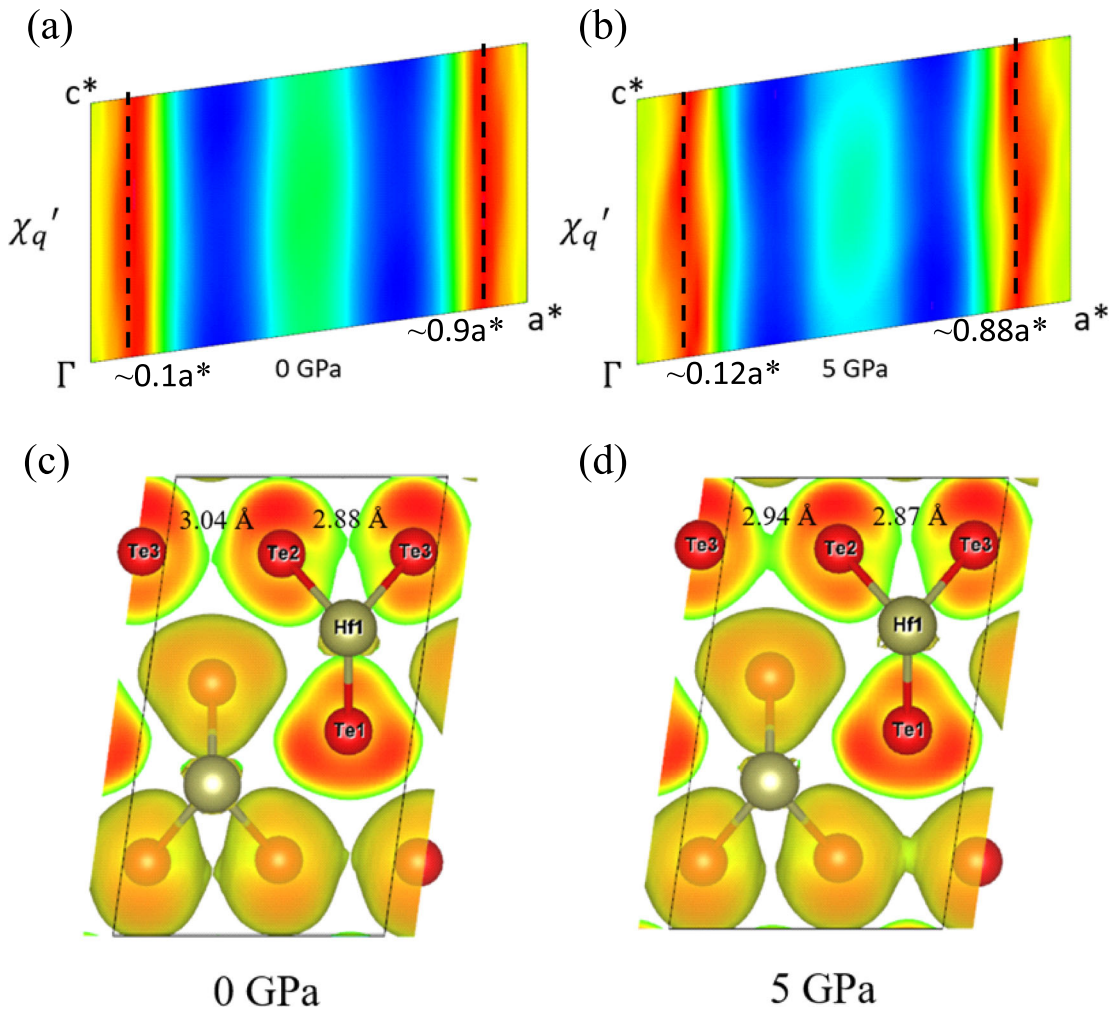


Fig. 9 The calculated electronic susceptibility and localization function of HfTe_3 . The calculated real part of the electronic susceptibility χ_q' for HfTe_3 in the a^* - c^* plane at **a** 0 GPa and **b** 5 GPa. The components along the b^* direction have been integrated. The calculated electronic localization function of HfTe_3 at **c** 0 GPa and **d** 5 GPa. The isosurface was set as 0.5.

pressure with a ratio of $k_{9 \text{ GPa}} : k_{11 \text{ GPa}} : k_{12.5 \text{ GPa}} = 2.4 : 1.4 : 1$. As shown in Fig. 3e, the T_c in the investigated pressure range only changes slightly, and thus the change of $\xi(0)$ should not dominate the significant decrease of the slope or the pre-factor of the above Eq. (2). Instead, the reduction of the slope should be mainly attributed to the increase of the diameter d of the superconducting filaments under pressure. This is conceivable considering the fact that the superconducting filaments are getting closer under HP. It can be expected that the superconducting state will gradually evolve into three dimensions under higher pressure or lower temperatures where the Josephson coupling between filaments is strengthened.

Before discussing the possible origins for the observed Q1D SC in the pressurized HfTe_3 , it is imperative to understand the nature of the CDW transition and its interplay with SC. A side-by-side comparison between HfTe_3 and ZrTe_3 is instructive. At ambient pressure, ZrTe_3 and HfTe_3 exhibit a CDW transition at $T_{\text{CDW}} = 63$ and 93 K, respectively. The determined CDW vector of HfTe_3 , i.e., $\mathbf{q} = 0.91(1) a^* + 0.27(1) c^*$ is very similar to that of ZrTe_3 , i.e., $\mathbf{q} = 0.93 a^* + 0.33 c^*$. In general opinion, the CDW vector is related to both the FS nesting vector and the electron-phonon coupling distribution. As shown in Fig. 9, the calculated electronic susceptibility χ_q' of HfTe_3 demonstrates an obvious peak at $0.90 a^*$, which is in excellent agreement with the experimental result determined from the TEM measurements. Nevertheless, there is no obvious peak along

the c^* direction, so it is difficult to determine the c^* component of \mathbf{q} merely based on the information of FS nesting. We suspect that the electron-phonon coupling in HfTe_3 may play a dominant role in the c^* component of its CDW vector. The calculated electronic susceptibilities of ZrTe_3 under 0 and 5 GPa are shown in Supplementary Fig. 13 for comparison. The red regions were drawn by the contour line of calculated electronic susceptibility χ_q' , while the experimentally determined CDW vectors \mathbf{q} were also labeled. Obviously, the c^* components of experimental \mathbf{q} do not correspond to the peaks of calculated χ_q' , while their a^* components seem to be well matched. This is similar to the above case of HfTe_3 .

Below T_{CDW} , an anisotropic superconducting transition was discovered in ZrTe_3 .^{5,13} In specific, ρ_a starts to decrease at $T_c^{\text{onset}} \approx 4$ K and reaches zero at $T_c^{\text{zero}} \approx 2$ K with a relatively broad superconducting transition, while ρ_b exhibits a much narrower transition from $T_c^{\text{onset}} \approx 2$ K to $T_c^{\text{zero}} \approx 1.5$ K. Based on the specific-heat measurements, the observed anisotropic superconducting transition has been ascribed to a gradual crossover from a filamentary SC (between 4 and 2 K) induced by local pairs along the a -axis to a bulk SC (below 1.5 K) when the superconducting filaments form phase coherence¹³. Such a mixed bulk-filament SC observed in ZrTe_3 has been attributed to the peculiar electronic structures characterized by the presence of Q1D and 3D FSs^{10,13,19}. In striking contrast to ZrTe_3 , no SC was detected down to 50 mK for the high-quality HfTe_3 single crystals². Their distinct

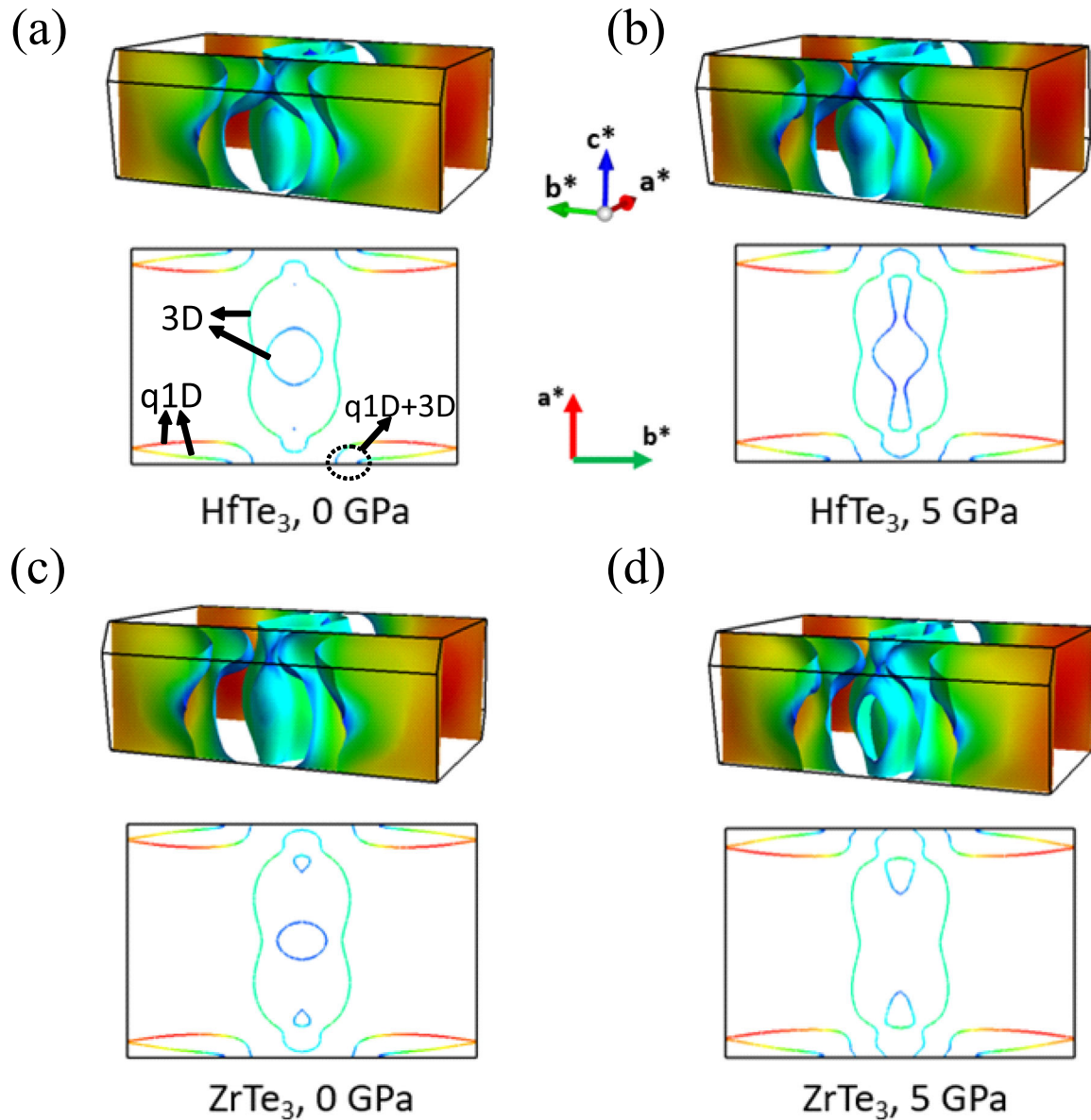


Fig. 10 Pressure effect on the Fermi surfaces of HfTe_3 and ZrTe_3 . The calculated Fermi surface sheets of **a, b** HfTe_3 and **c, d** ZrTe_3 at 0 GPa and 5 GPa, respectively. The color scales on the Fermi surface represent the Fermi velocities, where the pure red and pure blue correspond to the highest and zero Fermi velocities, respectively. The bottom figures in each panel are the sections of Fermi surface sheets at the $c^* = 0$ plane.

low-temperature behaviors can be rationalized by comparing to the effects of physical pressure on the CDW and SC of ZrTe_3 . At ambient conditions, the cell volume of HfTe_3 (228.70 \AA^3) is about 1.35% smaller than that of ZrTe_3 (231.83 \AA^3)^{8,20}, which corresponds to the application of 0.84 GPa hydrostatic pressure on ZrTe_3 given compressibility of 0.016 GPa^{-1} ¹⁴. At this pressure, it was found that the CDW transition of ZrTe_3 is enhanced to ca. 100 K while the SC is suppressed completely^{19,22}, which are similar to the situations seen in HfTe_3 at ambient pressure.

The above simple arguments indicate that the coexistent CDW and SC in ZrTe_3 at ambient pressure are actually competing with each other, which becomes more evident under pressure. For ZrTe_3 , a reentrant SC emerges above 5 GPa when the CDW disappears abruptly; the observed SC was believed to be bulk in nature¹⁷, but the diamagnetic evidence is still lacking to date as mentioned above¹². In the present case, we observed similar pressure-induced SC in R_g of HfTe_3 , but the absences of SC along the other directions and the absence of diamagnetic signals point to an intrinsic filamentary character for the observed SC. Our work

thus calls for a reexamination of the anisotropic properties of ZrTe_3 under high pressures. Our DFT calculations also provide some clues for the suppression of CDW under pressure. As shown in Fig. 9c, d, the distances between the Te2 and Te3 atoms in the -Te2-Te3- chain along the a -axis becomes more uniform at high pressures. In addition, there are more localized electrons between the Te2 and Te3 atoms from different prismatic $(\text{HfTe}_3)_\infty$ chains.

Finally, we discuss the possible origins for the observed extremely anisotropic or Q1D SC in the pressurized HfTe_3 according to the proposal by Yamaya et al.¹³ Similar to ZrTe_3 ^{8,9}, our electronic structure calculations show that HfTe_3 owns both 3D FSs around the BZ center and Q1D FSs around the BZ boundary, as shown in Fig. 10a. The former ones are dominated by Hf 5d orbitals in the $(\text{HfTe}_3)_\infty$ prism, while the latter ones are mainly contributed by unidirectional Te-5p_x orbitals within the -Te2-Te3-Te2-Te3- chain along the a -axis, Fig. 1a. At the intersection area between these two types of FSs, there are also Q1D + 3D FSs as indicated by the black arrows in Fig. 10a. On these FSs, the Fermi velocities are displayed with the color scales,

where the red and blue colors represent the highest and zero Fermi velocities, respectively. In particular, the low Fermi velocities near the Q1D + 3D FSs with the narrow-band feature may result in van Hove singularity (vHs) in the density of states. It is known that the presence of a vHs at E_F can induce FS instabilities and lead to SC or CDW states. In the narrow bands that construct the Q1D + 3D FSs, electrons can form local pairs that interact attractively with each other over short distances¹³. With increasing pressure, as shown in Fig. 10b, the 3D FSs of HfTe₃ around the Brillouin zone center expand, which enhance their overlapping with the Q1D FSs and reduce the composition of the Q1D bands at the Fermi level. As a result, the FS nesting of Q1D FSs along the a^* direction is weakened under pressure, which may suppress the CDW order and induce the SC. Since the narrow-band electron of HfTe₃ also has a dominant Te-5 p_x characteristic originating in the -Te2-Te3-chains as in ZrTe₃, the local pairs must be dominantly formed along the a -axis, leading to the Q1D SC transition in the a -axis direction¹⁹. In comparison, the 3D FSs of ZrTe₃ are larger than those of HfTe₃ at 0 GPa and even become the open-orbital pockets along the a^* direction at 5 GPa, as shown in Fig. 10c, d. This indicates that the CDW order due to the Q1D FSs nesting in ZrTe₃ is not so strong as in HfTe₃, which is consistent with the tendency of the experimental T_{CDW} of ZrTe₃ (63 K)⁶ versus HfTe₃ (93 K). Therefore, the anisotropic SC property in HfTe₃ can maintain in a wider temperature/pressure range, which makes HfTe₃ an ideal platform to study the local pairs in the Q1D superconducting system.

In summary, we have measured the anisotropic resistances of the CDW conductor HfTe₃ under high pressures. We found that a Q1D SC emerges in $R_a(T)$ at $T < 4\text{--}5$ K when the CDW is suppressed completely by $P > 5$ GPa, whereas no clear sign of SC is observed down to 1.4 K in $R_b(T)$ and $R_c(T)$. Our results demonstrate an intimate interplay between CDW and SC in HfTe₃, which are particularly interesting given their Q1D characters. We have compared our results with those of ZrTe₃ and discussed the pressure-induced Q1D SC in pressurized HfTe₃ in terms of the peculiar electronic structures and the local pairs formed along the -Te2-Te3- chains parallel to the a -axis.

METHODS

Single-crystal growth and characterization

High-quality HfTe₃ single crystals used in the present study were grown with the iodine chemical-vapor-transport method as described elsewhere². Before HP measurements, the crystals have been carefully characterized at ambient pressure by single-crystal X-ray diffraction (XRD), energy dispersive spectroscopy (EDS), TEM, and resistivity measurements. The CDW vector q at ambient pressure was determined by TEM measurements at 26 K. The specimens for TEM observation were prepared by mechanical exfoliation at room temperature and then transfer onto the Cu grid with the aid of crystal bond and acetone. In situ, low-temperature TEM experiments were performed using a liquid-helium-cooled specimen holder (GATAN, HCHDT3010) in a JEM-2100F electron microscope equipped with a charge-coupled device (CCD) camera system and operated at 200 keV.

Details of high-pressure measurements

The temperature dependences of resistance $R(T)$ under various pressures were measured with the standard four-probe method by using either a self-clamped piston-cylinder cell (PCC)²⁴ in the pressure range $0 < P \leq 2$ GPa or a palm-type cubic anvil cell (CAC)²⁵ in the pressure range $2 < P \leq 12.5$ GPa. In order to improve the electrical contact, we first evaporated four gold pads on the sample surface in a vacuum and then attached four gold wires of 20 μm in diameter on top of the gold pads with the silver paste. AC magnetic susceptibility under pressure has been measured with the mutual induction method. The excitation and pick-up coils are made of enameled copper wires of 25 μm in diameter, and they were manually wound around a Teflon sheet with a rectangular cross-section of 0.3 mm \times 0.5 mm. The Teflon sheet can be removed easily and the rectangular space ensures a large filling factor for the susceptibility measurements. Each coil

has two layers and about 40 turns in total. The HfTe₃ sample and a piece of lead (Pb) with a similar size of about 0.3 mm \times 0.3 mm \times 0.25 mm were put inside the pick-up coil. An excitation current of 1 mA with a frequency of 1117 Hz was applied to the excitation coil and the output signal was picked up with a Stanford Research SR830 lock-in amplifier. For these HP measurements, the Daphne 7373 or glycerol was employed as the pressure transmitting medium. The pressure in PCC was determined from the superconducting transition temperature of Pb, while the pressure in CAC was estimated from the calibration curve at low temperatures²⁶. High-pressure synchrotron powder XRD ($\lambda = 0.6199 \text{ \AA}$) was performed at room temperature at 4W2 beamline, Beijing Synchrotron Radiation Facility (BSRF). Silicone oil was used as the transmitting medium. The Le Bail method was employed to fit the XRD data with the General Structure Analysis System (GSAS) package program²⁷. The ruby fluorescence method was used to determine the pressure.

Theoretical calculations

To investigate the electronic structures of HfTe₃ under pressure, we carried out density functional theory (DFT) calculations with the projector augmented wave method^{28,29} as implemented in the VASP package^{30–32}. The generalized gradient approximation of Perdew–Burke–Ernzerhof (PBE) type³³ was adopted for the exchange–correlation functional. The kinetic energy cutoff of the plane wave basis was set to 300 eV. A $16 \times 16 \times 8$ k -point mesh was used for the Brillouin zone (BZ) sampling. The Fermi surface was broadened by the Gaussian smearing method with a width of 0.05 eV. The spin–orbit coupling effect was included as both Hf and Te are heavy elements. The vdW interaction was described by the optB86b-vdW functional³⁴. In the structural optimization, both cell parameters and internal atomic positions were allowed to relax until the forces on all atoms were smaller than 0.01 eV/ \AA . The Fermi surface (FS) and Fermi velocity of HfTe₃ were studied with the Wannier90³⁵ and FermiSurfer³⁶ packages, respectively. To describe the Fermi surface nesting, the real part of electronic susceptibility

χ_q' ($\chi_q' = \sum_{\mathbf{k}, j} \frac{f(\epsilon_{\mathbf{k}+\mathbf{q},j}) - f(\epsilon_{\mathbf{k},j})}{\epsilon_{\mathbf{k},j} - \epsilon_{\mathbf{k}+\mathbf{q},j}}$) was computed, where $f(\epsilon_{\mathbf{k},j})$ is the Fermi-Dirac distribution function and $\epsilon_{\mathbf{k},j}$ is the energy of band i at vector \mathbf{k} .

DATA AVAILABILITY

The datasets generated during and/or analyzed during the current study are available from the corresponding author on reasonable request.

Received: 4 June 2021; Accepted: 16 October 2021;

Published online: 10 November 2021

REFERENCES

- Gruner, G. *Density waves in solids* (CRC Press, 1994).
- Li, J., Peng, J., Zhang, S. & Chen, G. F. Anisotropic multichain nature and filamentary superconductivity in the charge density wave system HfTe₃. *Phys. Rev. B* **96**, 174510 (2017).
- Takahashi, S., Sambongi, T. & Okada, S. Conduction properties of ZrTe₃. *J. Phys. Colloq.* **44**, 1733–1736 (1983).
- Takahashi, S., Sambongi, T., Brill, J. W. & Roark, W. Transport and elastic anomalies in ZrTe₃. *Solid State Commun.* **49**, 1031–1033 (1984).
- Nakajima, H., Nomura, K. & Sambongi, T. Anisotropic superconducting transition in ZrTe₃. *Phys. Rev.* **143B**, 240–242 (1986).
- Eaglesham, D. J., Steeds, J. W. & Wilson, J. A. Electron microscope study of superlattices in ZrTe₃. *J. Phys. C Solid State Phys.* **17**, L697–L698 (1984).
- Furuseth, S. & Fjellvag, H. Reexamination of the crystal-structure of ZrTe₃. *Acta Chem. Scand.* **45**, 694–697 (1991).
- Stowe, K. & Wagner, F. R. Crystal structure and calculated electronic band structure of ZrTe₃. *J. Solid State Chem.* **13B**, 160–168 (1998).
- Felsner, C., Finckh, E. W., Kleinke, H., Rocker, F. & Tremel, W. Electronic properties of ZrTe₃. *J. Mater. Chem.* **8**, 1787–1798 (1998).
- Yokaya, T., Kiss, T., Chainani, A., Shin, S. & Yamaya, K. Role of charge-density-wave fluctuations on the spectral function in a metallic charge-density-wave system. *Phys. Rev. B* **71**, 140504 (2005).
- Hoesch, M. et al. Splitting in the Fermi surface of ZrTe₃: a surface charge density wave system. *Phys. Rev. B* **80**, 075423 (2009).
- Yomo, R., Yamaya, K., Abliz, M., Hedo, M. & Uwatoko, Y. Pressure effect on competition between charge density wave and superconductivity in ZrTe₃: appearance of pressure-induced reentrant superconductivity. *Phys. Rev. B* **71**, 132508 (2005).

13. Yamaya, K., Takayanagi, S. & Tanda, S. Mixed bulk-filament nature in superconductivity of the charge-density-wave conductor $ZrTe_3$. *Phys. Rev. B* **85**, 184513 (2012).
14. Hoesch, M., Garbarino, G., Battaglia, C., Aebi, P. & Berger, H. Evolution of the charge density wave superstructure in $ZrTe_3$ under pressure. *Phys. Rev. B* **93**, 125102 (2016).
15. Zhu, X. D., Lei, H. C. & Petrovic, C. Coexistence of bulk superconductivity and charge density wave in Cu_xZrTe_3 . *Phys. Rev. Lett.* **106**, 246404 (2011).
16. Lei, H. C., Zhu, X. D. & Petrovic, C. Raising T_c in charge density wave superconductor $ZrTe_3$ by Ni intercalation. *Europhys. Lett.* **95**, 17011 (2011).
17. Zhu, X. Y. et al. Disorder-induced bulk superconductivity in $ZrTe_3$ single crystals via growth control. *Phys. Rev. B* **87**, 024508 (2013).
18. Zhu, X. D. et al. Superconductivity and charge density wave in $ZrTe_{3-x}Se_x$. *Sci. Rep.* **6**, 26974 (2016).
19. Tsuchiya, S. et al. Effects of pressure and magnetic field on superconductivity in $ZrTe_3$: local pair-induced superconductivity. *N. J. Phys.* **19**, 063004 (2017).
20. Denholme, S. J. et al. Coexistence of superconductivity and charge-density wave in the quasi-one-dimensional material $HfTe_3$. *Sci. Rep.* **7**, 45217 (2017).
21. Aslamazo, L. G. & Larkin, A. I. Influence of fluctuation pairing of electrons on conductivity of normal metal. *Phys. Lett.* **26A**, 238–239 (1968).
22. Yamaya, K., Yoneda, M., Yasuzuka, S., Okajima, Y. & Tanda, S. The effect of pressure on the charge-density wave and superconductivity in $ZrTe_3$. *J. Phys.: Condens. Matter* **14**, 10767 (2002).
23. Imada, M. & Scalapino, D. J. Competition between the charge-density-wave and singlet-superconducting phases in a quasi-one-dimensional system. *Phys. Rev. B* **34**, 3480 (1986).
24. Uwatoko, Y. Design of a piston cylinder type high-pressure cell. *Rev. High. Press. Sci. Tech.* **12**, 306–311 (2002).
25. Uwatoko, Y. et al. Development of palm cubic anvil apparatus for low temperature physics. *Rev. High. Press. Sci. Tech.* **18**, 230–236 (2008).
26. Cheng, J. G. et al. Integrated-fin gasket for palm cubic-anvil high pressure apparatus. *Rev. Sci. Instrum.* **85**, 093907 (2014).
27. Larson, A. C. & Von Dreere, R. B. *General structure analysis system*. Report No. LAUR 86-748 (Los Alamos National Laboratory, 2004).
28. Blöchl, P. E. Projector augmented-wave method. *Phys. Rev. B* **50**, 17953 (1994).
29. Kresse, G. & Joubert, D. From ultrasoft pseudopotentials to the projector augmented-wave method. *Phys. Rev. B* **59**, 1758 (1999).
30. Kresse, G. & Hafner, J. Ab initio molecular dynamics for liquid metals. *Phys. Rev. B* **47**, 558 (1993).
31. Kresse, G. & Furthmüller, J. Efficiency of ab-initio total energy calculations for metals and semiconductors using a plane-wave basis set. *Comp. Mater. Sci.* **6**, 15 (1996).
32. Kresse, G. & Furthmüller, J. Efficient iterative schemes for ab initio total-energy calculations using a plane-wave basis set. *Phys. Rev. B* **54**, 11169 (1996).
33. Perdew, J. P., Burke, K. & Ernzerhof, M. Generalized gradient approximation made simple. *Phys. Rev. Lett.* **77**, 3865 (1996).
34. Klimeš, J., Bowler, D. R. & Michaelides, A. Chemical accuracy for the van der Waals density functional. *J. Phys.: Condens. Matter* **22**, 022201 (2010).
35. Mostofi, A. A. et al. Wannier90: a tool for obtaining maximally-localised Wannier functions. *Comp. Phys. Commun.* **178**, 685–699 (2008).
36. Kawamura, M. FermiSurfer: Fermi-surface viewer providing multiple representation schemes. *Comp. Phys. Commun.* **239**, 197–203 (2019).

ACKNOWLEDGEMENTS

We are grateful for the enlightening discussions with Prof. Jianshi Zhou and Dr. Jiaqiang Yan. This work is supported by the Beijing Natural Science Foundation

(Z190008), National Natural Science Foundation of China (12025408, 11921004, 11888101, 11834016, 11904391, 11874400, and 11774424), the National Key R&D Program of China (2018YFA0305702, 2018YFA0305800, and 2017YFA0302903), the Strategic Priority Research Program and Key Research Program of Frontier Sciences of the Chinese Academy of Sciences (XDB25000000, XDB33000000, and QYZDB-SSW-SLH013), and the CAS Interdisciplinary Innovation Team (JCTD-2019-01) as well as the Users with Excellence Program of Hefei Science Center CAS (Grant No. 2021HSC-UE008). Y.U. acknowledges the support from JSPS KAKENHI (19H00648). ADXRD measurements were performed at 4W2 High-Pressure Station, Beijing Synchrotron Radiation Facility (BSRF), which is supported by the Chinese Academy of Sciences (Grant KJCX2-SW-N20 and KJCX2-SW-N03).

AUTHOR CONTRIBUTIONS

J.-G.C. directed this research. J.L., S.Z., and G.F.C. grew the $HfTe_3$ single crystals. Z.Y.L. and P.T.Y. performed the high-pressure measurements and data analyses. J.L. and H.X.Y. carried out the TEM measurements and data analysis. Y.U. provided the high-pressure methodology. J.F.Z. and K.L. did the electronic structure calculations. Z.Y.L., K.L., Y.S., and J.-G.C. wrote this manuscript with comments from all authors. Z.Y.L., J.L., and J.F.Z. contributed equally to this work.

COMPETING INTERESTS

The authors declare no competing interests.

ADDITIONAL INFORMATION

Supplementary information The online version contains supplementary material available at <https://doi.org/10.1038/s41535-021-00393-8>.

Correspondence and requests for materials should be addressed to S. Zhang, Y. Sui, K. Liu or J.-G. Cheng.

Reprints and permission information is available at <http://www.nature.com/reprints>

Publisher's note Springer Nature remains neutral with regard to jurisdictional claims in published maps and institutional affiliations.



Open Access This article is licensed under a Creative Commons Attribution 4.0 International License, which permits use, sharing, adaptation, distribution and reproduction in any medium or format, as long as you give appropriate credit to the original author(s) and the source, provide a link to the Creative Commons license, and indicate if changes were made. The images or other third party material in this article are included in the article's Creative Commons license, unless indicated otherwise in a credit line to the material. If material is not included in the article's Creative Commons license and your intended use is not permitted by statutory regulation or exceeds the permitted use, you will need to obtain permission directly from the copyright holder. To view a copy of this license, visit <http://creativecommons.org/licenses/by/4.0/>.

© The Author(s) 2021